

Improving the Adhesion of a Hard Oxide Layer on Ti6Al4V by a Three-Step Thermal Oxidation Process

Daniel Dickes, Beyza Öztürk, Rainer Völkl, Mathias C. Galetz, and Uwe Glatzel*

Thermal oxidation is a promising technique to improve the tribological properties of Ti6Al4V. Herein, a single-step process consisting of oxidation in air, a two-step process with an additional solid-state oxide layer reduction step under vacuum, and a three-step process with an appended final oxidation step in air are applied to Ti6Al4V. The oxide layer adhesion after the three-step process is improved compared with the single-step process. This improved adhesion is not due to a different nature of the oxide layers because oxide layers obtained during the single-step and three-step process show a similar morphology and composition. Instead, it is ascribed to the presence of an optimized oxygen diffusion zone with two distinct regions: a gradual decrease in oxygen concentration from the maximum possible oxygen concentration at the oxide–substrate interface until a depth of 20 μm followed by a near-linear decrease until a depth of about 85 μm . Both regions are also visible in the correlated microhardness-depth profile.

whereby the composition and hardness of the oxide layers are dependent on the thermal oxidation process parameters.^[10–13] Such parameters are the oxidation duration, the temperature, the composition of the oxidizing atmosphere, and the partial pressure or the oxidant activity. An increase in duration or temperature leads to thicker oxide layers^[14–17] but goes along with an increased porosity,^[16] an increased surface roughness,^[12,13,18,19] and a decreased layer adherence.^[10,20,21] The latter are major problems in tribological applications, e.g., in implanted joints where wear debris and spalled of parts can cause inflammation.^[22]

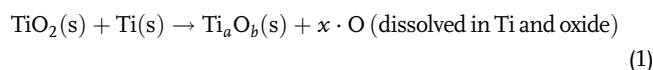
Due to the high oxygen solubility of up to 33.3 at. % in α -titanium,^[23] the oxide layer formation at elevated temperatures is accompanied by oxygen diffusion into the

substrate, leading to an oxygen diffusion zone.^[2]

Figure 1 shows a schematic oxygen concentration-depth profile obtained after thermal oxidation of commercially pure titanium, as modeled by Unnam et al.^[24] Starting at the oxide–substrate interface, the oxygen concentration decreases gradually in the oxygen diffusion zone until it reaches a constant concentration close to 0 at. %.^[24] The hardness in the oxygen diffusion zone also decreases gradually from the oxide–substrate interface toward the softer substrate because the oxygen concentration in Ti6Al4V is correlated with the material hardness.^[25] According to Güleriyüz et al.,^[2] such graded surfaces with good adhesion characteristics have the potential to improve the wear behavior of Ti6Al4V.

Different thermal oxidation processes have been deployed to optimize the tribological properties. The simplest concept is a single-step air oxidation, often conducted in a temperature range from 600 to 850 °C.^[12,14,16,26–33] Oxygen diffusion zones, and thus zones of a gradual hardness decrease, obtained by this process have depths generally much less than 100 μm .^[12,14,26–28] Reaching for thicker oxygen diffusion zones by single-step air oxidation is difficult because increasing the process temperature or the oxidation duration results in porous and less adherent oxide layers.^[13,15,16,27]

Oxygen diffusion zone depths of more than 100 μm can be achieved by adding a vacuum heat treatment step to the process.^[34–37] During this vacuum heat treatment, often performed at 850 °C,^[25,34–36] oxygen which is released by the reduction of TiO₂ diffuses into the substrate until the oxide layer is completely dissolved. According to Zhang et al.,^[35] two reactions are possible for this solid-state reduction of the oxide layer



1. Introduction

Ti6Al4V is the most widely used titanium alloy with applications ranging from aerospace engineering to health technology.^[1] While titanium alloys show excellent mechanical properties, good corrosion resistance, and biocompatibility, their tribological properties are described as poor.^[2–4] To overcome this drawback, numerous surface modification techniques have been investigated.^[4–8] A promising approach to improve the tribological properties of Ti6Al4V is thermal oxidation. Thermal oxidation is defined as the growth of an oxide layer on a substrate during heat exposure in an oxidizing atmosphere.^[9] The oxide layer forming on Ti6Al4V mainly consists of TiO₂, in the form of rutile or anatase, and has an increased hardness compared with the substrate,

D. Dickes, R. Völkl, U. Glatzel
Metals and Alloys
University of Bayreuth
Prof.-Rüdiger-Bormann-Straße 1, Bayreuth 95447, Germany
E-mail: uwe.glatzel@uni-bayreuth.de

B. Öztürk, M. C. Galetz
High Temperature Materials
DEHEMA-Forschungsinstitut
Theodor-Heuss-Allee 25, Frankfurt am Main 60486, Germany

The ORCID identification number(s) for the author(s) of this article can be found under <https://doi.org/10.1002/adem.202100864>.

© 2021 The Authors. Advanced Engineering Materials published by Wiley-VCH GmbH. This is an open access article under the terms of the Creative Commons Attribution License, which permits use, distribution and reproduction in any medium, provided the original work is properly cited.

DOI: 10.1002/adem.202100864

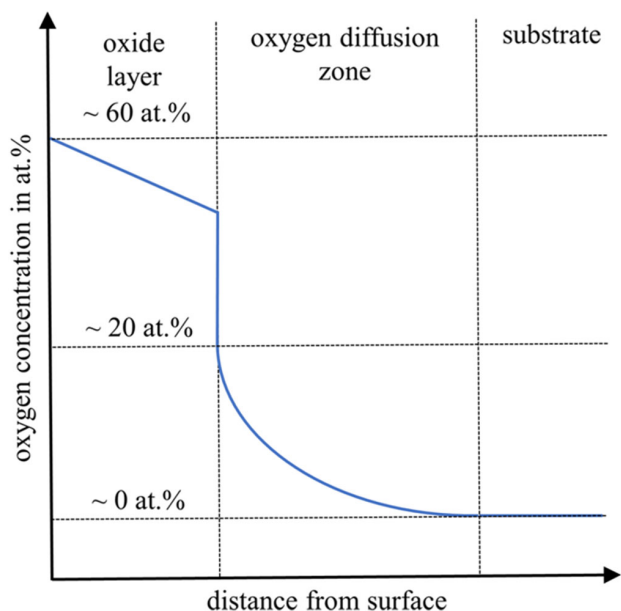


Figure 1. Schematic oxygen concentration-depth profile of a commercially pure titanium specimen after thermal oxidation. According to Unnam et al.^[24]



Ti6Al4V treated with such a two-step process, also referred to as oxygen boost diffusion,^[34,38] shows an increased surface hardness and a better wear resistance in fretting mode but lacks a protective oxide layer, which is essential when it comes to corrosion resistance and biocompatibility.^[39] To obtain an oxide layer in combination with a pronounced oxygen diffusion zone, Rastkar et al.^[40] proposed a three-step process consisting of the steps: oxidation in air, oxide layer reduction in vacuum, and an additional oxidation in air. For zirconium alloys, such a process was implemented to improve the oxide layer adhesion.^[41,42] Bacroix et al.^[39] applied this three-step process also to Ti6Al4V, focusing on the effect of different oxidation temperatures during the first oxidation step on tribological properties. A diffusion zone of approximately 600 μm could be reached and parameters leading to an improved wear resistance were identified.

This work aims to demonstrate that the three-step process can also be used to improve the oxide layer adhesion already at far smaller diffusion depths due to the formation of two distinct regions in the diffusion zone: a gradual oxygen concentration decreases from its maximum at the oxide–substrate interface followed by a near-linear decrease deeper toward the substrate. As the nature of oxide layers obtained during the three-step process has not been explicitly characterized to the authors' knowledge, this work includes a comparative study of the surfaces after the single-step, two-step, and three-step process to consider a potential influence of the nature of the obtained oxide layer on its adhesion.

2. Materials and Methods

In this study, 2 mm-thick, annealed Ti6Al4V sheet material according to AMS 4911 was used. Specimens of 10 mm × 20 mm size were cut from sheet material, ground with P500 and P1200 abrasive paper, and cleaned ultrasonically in ethanol.

Figure 2 shows a backscattered scanning electron microscopy image of the cross-sectional microstructure in the initial state. The brighter appearing β-phase is homogeneously distributed in the specimen. Grains of the β-phase are narrow and exhibit directionality as the specimens are from a rolled sheet.

Table 1 shows the thermal oxidation treatment process parameters of the single-step, two-step, and three-step process. During each process step, the specimens were placed in a preheated chamber furnace followed by air cooling after the respective thermal oxidation treatment duration. To realize the low vacuum atmosphere during the second process step, specimens were encapsulated in evacuated quartz glass tubes. This limits the available amount of oxygen for further oxidation of the encapsulated specimens and promotes the solid-state oxide layer reduction.

The thermal oxidation-treated specimens were either analyzed in the as-treated state or after metallographic cross-sectional preparation. For a surface analysis via scanning electron microscopy (SEM), a Zeiss 1540 ESB Cross Beam with an Everhart–Thornley and an inlens secondary electron (SE) detector as well as a semiconductor and an inlens backscattered electron (BSE) detector was used. Elemental analysis was performed with a Thermo Noran System Six energy-dispersive X-ray spectroscopy (EDS) system with a silicon drift detector. In addition, an X-ray diffraction analysis (XRD) was conducted on a Bruker D8 Discovery. A diffraction angle range from 20° to 80° was analyzed with a step size of 0.01° and a count time of 0.5 s under

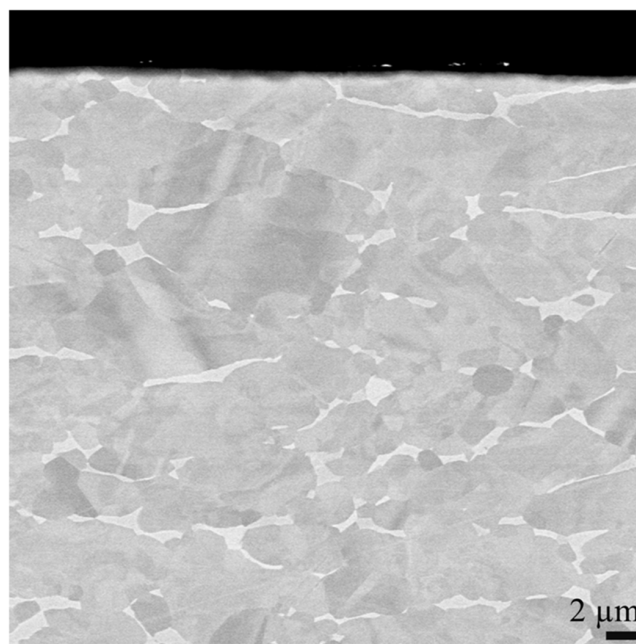


Figure 2. Microstructure of a Ti6Al4V specimen in the initial state after grinding.

Table 1. Process parameters used during the single-step, two-step, and three-step thermal oxidation process.

Process step	Three-step process		
	Two-step process		
	Single-step process		
Oxidation in air		Oxide reduction	Oxidation in air
Duration in h	16	6	16
Temperature in °C	680	850	680
Atmosphere	Air at atmospheric pressure (1×10^5 Pa)	Low vacuum (4×10^3 Pa) in sealed glass tube (≈ 10 cm ³)	Air at atmospheric pressure (1×10^5 Pa)

Cu $K\alpha_1$ radiation. Glow discharge optical emission spectroscopy (GDOES) was used to obtain elemental concentration-depth profiles. Measurements were performed on a Spectrumba GDA alpha with a suitable calibration to quantify oxygen. An effective initial oxygen concentration of 20 at. % at the oxide–substrate interface, as proposed by Unnam et al.^[24] and confirmed in preliminary tests, was chosen to distinguish between oxide layer and substrate if an oxide layer was present. The roughness parameters R_a and R_z were determined according to ISO 4288 with a MarSurf PS 10 profilometer. Twelve roughness measurements per specimen were used to calculate an average. The morphology and thickness of the oxide layers were analyzed via SEM of the prepared cross sections. Eight different backscattered electron images per cross section were considered to average the oxide layer thickness of every specimen. Each image, evaluated at more than 100 positions, represented an oxide layer length of approximately 50 μm with a resolution of ≈ 0.05 μm . Depth-controlled Martens hardness measurements were performed on a Fischerscope H100 using a Vickers indenter and an indentation depth of 0.2 μm . Up to 400 measurement points were used to derive microhardness-depth profiles down to a depth of 100 μm in the substrate. The layer adhesion was assessed through Rockwell indentation tests specified in EN ISO 26 443 (diamond indenter, 60 kg load, 10 s duration).

3. Experimental Results

Optical inspection with the naked eye reveals a dark brownish surface on specimens after the single-step and three-step process (Figure 3). In contrast to that, the surface after the two-step process has a bright, mat, metallic appearance with some impurities.

SEM images at high magnification of specimens exposed to the single-step process (Figure 4a–c) show agglomerations of oxide grains with a fine, elongated rod shape (arrow 1,

Figure 4a) and larger polyhedron-type grains (arrow 2) on the surface of the oxide layer. A third type of oxide grains without a clearly defined shape can be identified in-between the latter. After the two-step process, the fine, rod-shaped grains are no longer present. Instead, the surface consists of densely agglomerated polyhedron-type grains only. Some of those grains have a terraced structure (arrow 3, Figure 4b). The oxide layer obtained after the three-step process is similar to the one after the single-step process.

At a lower magnification (μm -scale, Figure 4d–f), the oxide layer obtained after the single-step process shows an uneven surface with elevated clusters of fine oxide grains (arrow 4, Figure 4d). Such clusters can still be identified after the two-step process (Figure 4e), even though the surface appears smoother. After the three-step process, elevated clusters of oxide grains appear again.

Table 2 shows the roughness parameters R_a and R_z measured after every process. The roughness measurements reflect the different extend of oxide grain cluster formation. Compared with the untreated specimen state (after grinding), the roughness is increased after the single-step process. The subsequent oxide layer reduction step leads to a decline of R_a and R_z . The surface after the three-step process has the highest roughness.

According to the XRD measurement shown in Figure 5, the oxide layer obtained via the single-step process mainly consists of TiO_2 rutile (ICDD 00–021–1276) and a small amount of $\alpha\text{-Al}_2\text{O}_3$ (ICDD 01–070–5679). Peaks indicating $\alpha\text{-Ti}$ (ICDD 00–044–1294) are present as well and can be related to the substrate underneath the oxide layer. After the two-step process, neither TiO_2 nor $\alpha\text{-Al}_2\text{O}_3$ can be identified in the XRD pattern. Instead, characteristic peaks of the surface and subsurface region are $\alpha\text{-Ti}$ and Ti_3Al (ICDD 00–052–0859). The XRD pattern of a specimen after the three-step process is similar to the single-step result.



Figure 3. Specimens after the single-step, two-step, and three-step process.

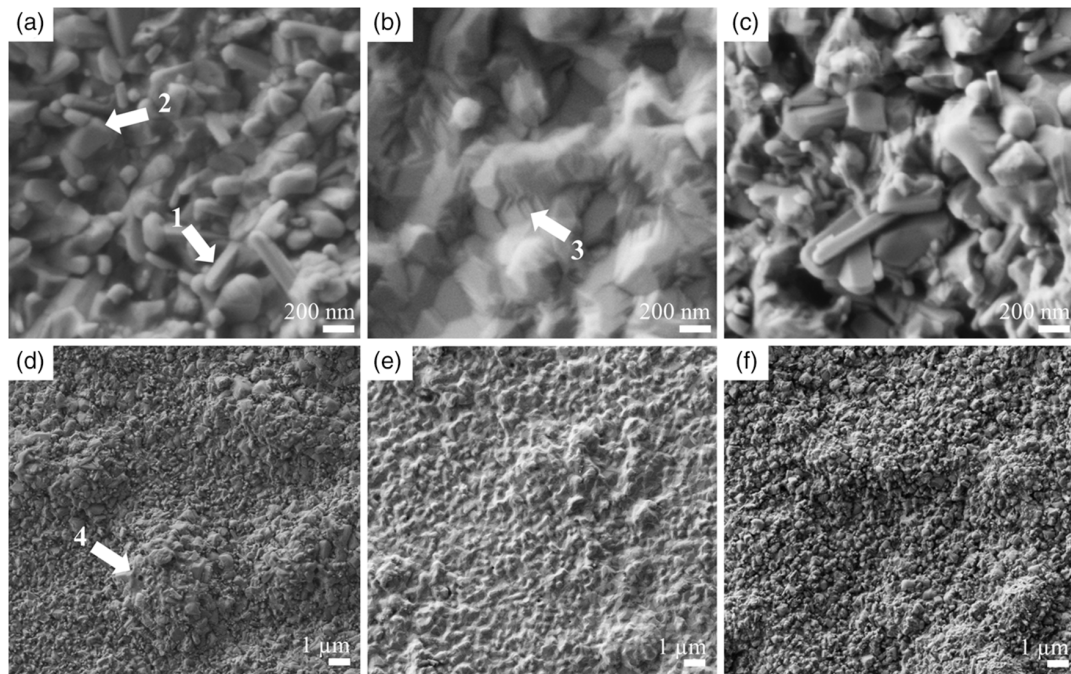


Figure 4. SE SEM images of surfaces obtained after the a,d) single-step, b,e) two-step, and c,f) three-step process on the nanometer and the micrometer scale.

Table 2. Mean roughness parameters R_a and R_z and standard deviation of the initial specimen and a specimen after the single-step, two-step, and three-step process.

	Untreated	Single-step	Two-step	Three-step
R_a in μm	0.049 ± 0.004	0.223 ± 0.005	0.157 ± 0.021	0.293 ± 0.029
R_z in μm	0.401 ± 0.029	1.658 ± 0.068	1.215 ± 0.132	2.146 ± 0.182

Figure 6 shows the EDS analysis of a specimen after the single-step process. According to this analysis, the elongated rod-shaped oxide grains and the polyhedron-type oxide grains contain titanium (arrows 1 and 2, Figure 6). The oxide grains without a specified geometry are rich in aluminum (arrow 3, Figure 6). Aluminum-containing oxide grains are only present in the first 500 nm of the oxide layer (arrow 4, Figure 6). They do not entirely cover the oxide layer but are located in between titanium-containing oxide grains.

After the oxide layer reduction at the end of the two-step process, small grains, no larger than 500 nm, with a relatively high aluminum content have formed at the surface (arrow 1, Figure 7).

Figure 8 shows that the oxide layer obtained after the three-step process is similar to the one after the single-step process. Aluminum-containing oxide grains (arrow 1, Figure 8) are present in between titanium-containing oxide grains at the top of the oxide layer.

Figure 9 shows an overview of the effects of the three different processes on the surface microstructure. The SEM cross-sectional images of the oxide layer obtained after the single-step process show that an agglomeration of oxide grains can lead to a

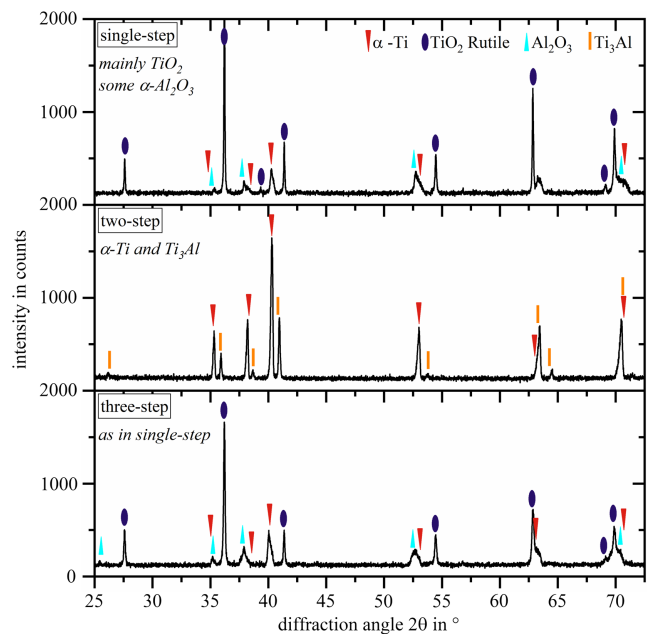


Figure 5. Characteristic XRD pattern of specimens after the single-step, two-step, and three-step process with identified peaks according to the ICDD database.

compact oxide layer in some regions, while open pores occur preferably close to the oxide–substrate interface (arrow 1, Figure 9a). In the substrate, elongated, brighter appearing grains of β -Ti (Figure 9d) similar to the initial state (Figure 2) can be identified.

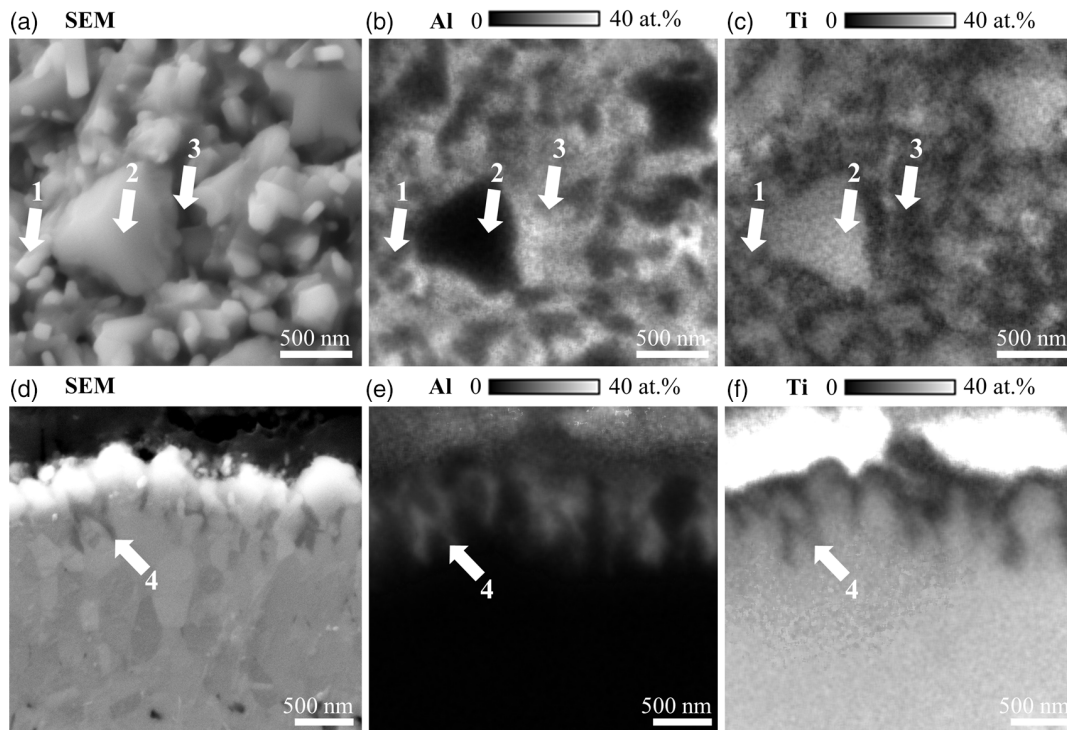


Figure 6. Top-view and cross-sectional SE SEM images of an oxide layer after the a,d) single-step process, with quantitative EDS mappings of b,e) aluminum and c,f) titanium.

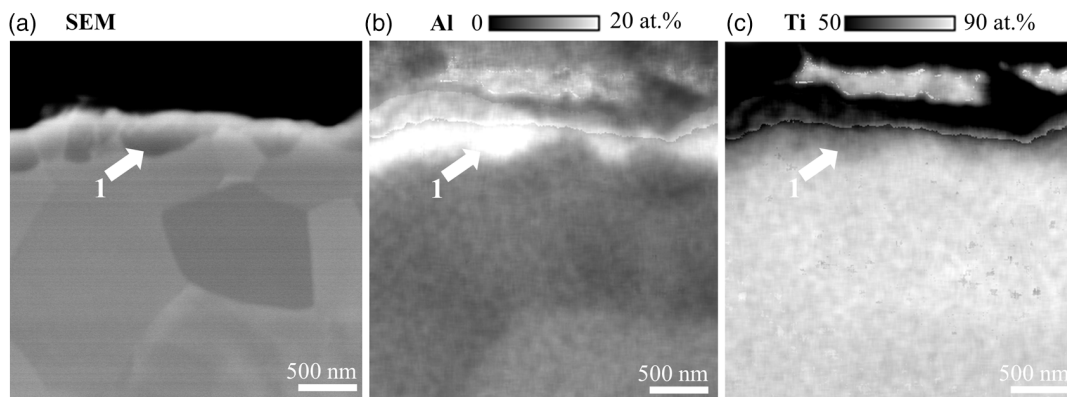


Figure 7. a) BSE SEM cross-sectional image of the surface after the two-step process, with quantitative EDS mappings of b) aluminum and c) titanium.

After the two-step process, no oxide layer is present (Figure 9b). Directly at the surface, the aluminum-rich grains, identified during the EDS analysis, appear as darker phases (arrow 3, Figure 9b). In some specimens, closed, round pores occur at a distance of approximately 1 μm from the surface (arrow 2, Figure 9b). In a similar depth, aluminum-rich darker phases tend to form zones with a lamellar structure (arrow 4, Figure 9b). No brighter appearing β -Ti phase is visible near the surface (arrow 5, Figure 9e). Compared with the single-step process, grain coarsening is observed in the substrate.

The oxide layer formed during the three-step process is similar to the one after the single-step process and possesses

pores close to the oxide–substrate interface (Figure 9c). The subsurface and substrate microstructure after the three-step process (Figure 9f) are similar to the ones after the two-step process.

Figure 10 shows the EDS mapping of the region with lamellar structure (arrow 4, Figure 9b). The lamella consists of phases rich in aluminum and titanium.

The average oxide layer thickness, derived from cross-sectional images, is shown in **Figure 11**. It is 2.6 μm after the single-step process and 3.3 μm after the three-step process. The thickness deviates within a range of $\pm 1.5 \mu\text{m}$ after the single-step process and $\pm 2 \mu\text{m}$ after the three-step process.

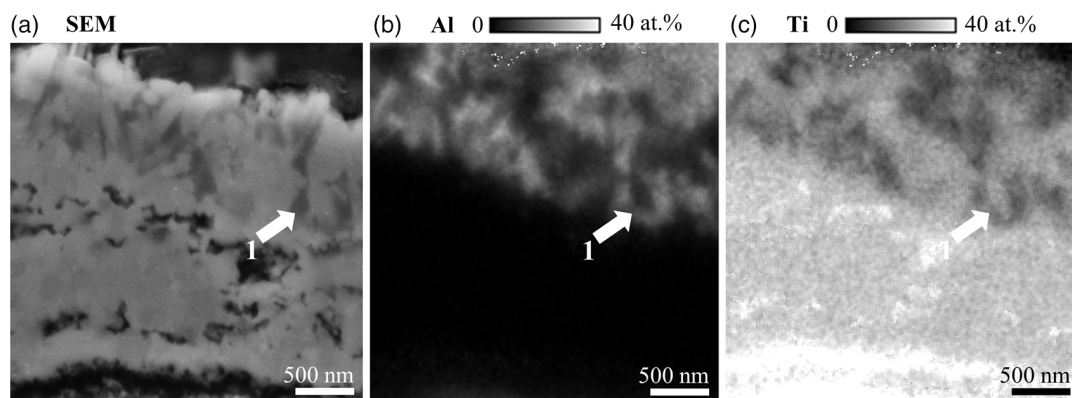


Figure 8. a) SE SEM cross-section image of an oxide layer after the three-step process, with quantitative EDS mappings of b) aluminum and c) titanium.

Figure 12 shows the oxygen concentration-depth profiles derived from GDOES measurements together with the microhardness depth-profiles in the oxygen diffusion zone starting at the oxide–substrate or the air–substrate interface.

In case of the single-step process, the oxygen concentration gradually decreases from the effective initial concentration of 20 at. % at the oxide–substrate interface until it reaches the constant concentration of 0 at. % at a depth of 20 μm .

For the two-step process, the initial concentration at the air–substrate interface is below 10 at. %. Higher oxygen concentrations measured in the first 0.5 μm in this case are caused by a GDOES measurement artifact. The constant substrate concentration of 0 at. % is not reached before a depth of 85 μm . Compared with the concentration profile after the single-step process, the gradient is lower during the first 15 μm but remains approximately constant, which leads to a near-linear behavior.

In the three-step process, the final oxidation step mainly affects a region of 20 μm close to the surface. The oxygen concentration gradually decreases from the effective initial concentration of 20 at. % at the oxide–substrate interface toward 5 at. % at approximately 20 μm . After that, the course is similar to the one after the two-step process, i.e., a near-linear decrease.

The microhardness-depth profiles behave as the oxygen concentration-depth profiles. Starting with an initial hardness of 9 GPa at the oxide–substrate interface, the hardness decreases strongly within the first 20 μm after the single-step process until it reaches the constant substrate hardness of ≈ 3.5 GPa.

The two-step process results in a reduced initial hardness of 6 GPa compared with the single-step process. After that, the hardness decreases in a near-linear manner to the substrate value of 3.5 GPa over a long distance of ≈ 85 μm .

The three-step process again leads to a high initial hardness of 9 GPa, which gradually decreases until a depth of approximately 20 μm down to ≈ 5.5 GPa. Then, the course is like the one obtained during the two-step process, i.e., a near-linear decrease down to the substrate hardness over a distance of ≈ 85 μm .

Based on all three oxygen concentration- and hardness-depth profiles, the relationship between oxygen concentration c_{oxygen} and microhardness HM in Ti6Al4V is best described by a parabolic relationship (**Figure 13**)

$$HM = HM_0 + b \cdot \sqrt{c_{\text{oxygen}}} \quad (3)$$

The initial substrate Martens hardness (0.2 μm depth controlled) HM_0 is 2.9 GPa at an oxygen concentration which is 0–0.2 wt. % according to AMS 4911. The coefficient b is 1.2 GPa. The applicability of such an empirical parabolic relationship between oxygen concentration and microhardness has been confirmed recently by Vaché and Monceau.^[43]

Figure 14 shows the results of the Rockwell indentation tests. The specimen in the initial state does not show any surface damage other than the indenter imprint (**Figure 14a**). Instead, the oxide layer obtained during the single-step process (**Figure 14b**) is completely delaminated and of class 3 according to EN ISO 26 443. Cracks of a few micrometers are observed in the subsurface region. After the two-step process (**Figure 14c**), cracks of approximately 200 μm length are visible around the indenter imprint. The oxide layer obtained during the three-step process (**Figure 14d**) is partially delaminated and of layer adhesion class 2. Segments of the oxide layer remain attached to the underlying substrate. This segmentation of the oxide layer is related to cracks in the subsurface region, similar to those observed after the two-step process.

4. Discussion

All three thermal oxidation processes are successfully implemented for Ti6Al4V. The presence of an oxide layer is detected by the visual surface appearance, SEM cross-section images, and XRD. The observations are shown in **Table 3**.

4.1. Constitution of Surface Grains

A quantitative EDS mapping, as performed by Dong et al.^[17] and Zhou et al.,^[36] in this work is combined with an XRD analysis to assign a characteristic phase even to grains of a few nanometers. The oxide layer after the single-step and three-step process consists of TiO₂ rutile grains, which, at the surface, can occur as elongated rods or polyhedrons. In the top 500 nm of the oxide layer, α -Al₂O₃ forms but does not entirely cover the oxide layer.

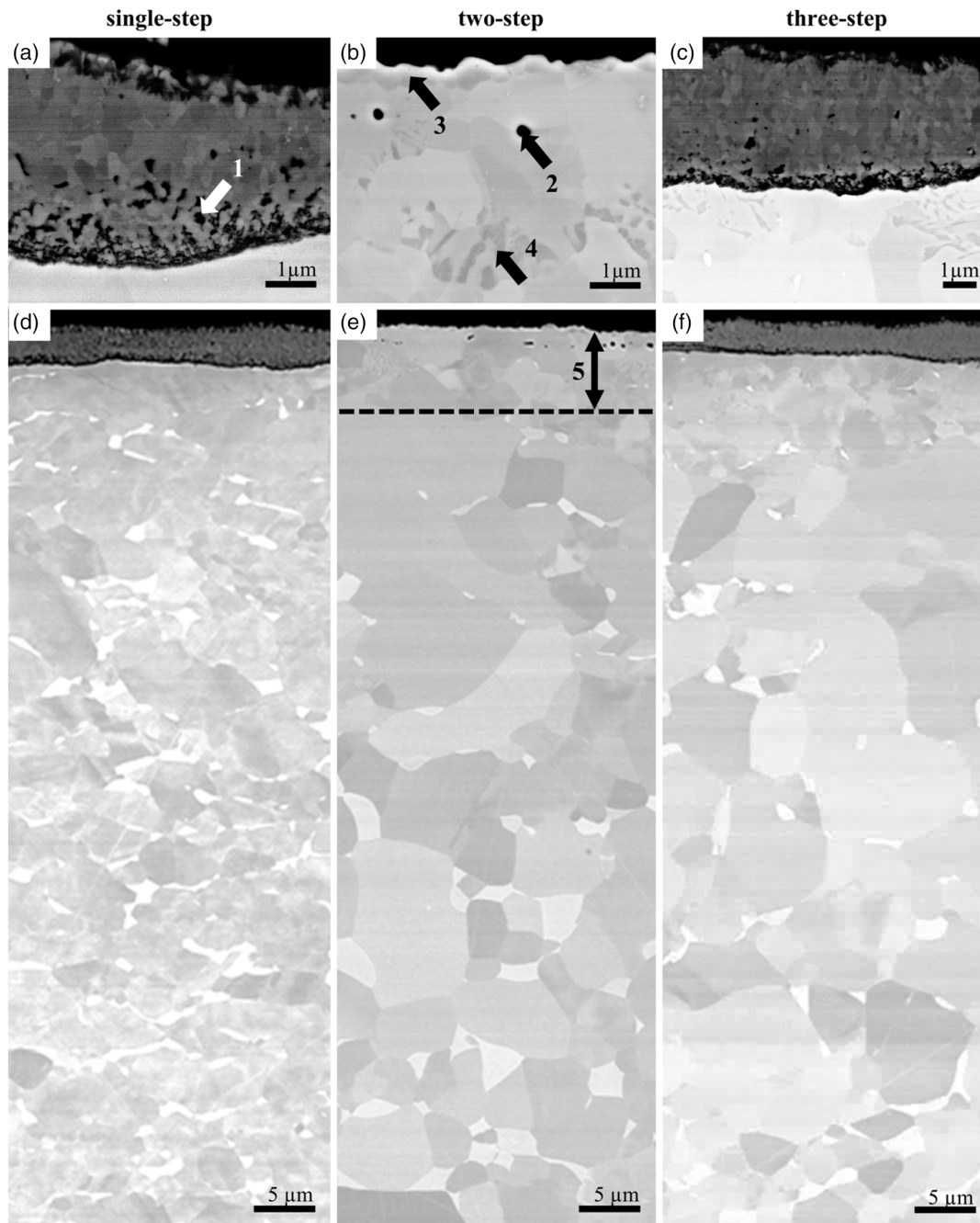


Figure 9. BSE SEM cross-sectional analysis of the surface and subsurface region of thermal oxidation treated specimens after the a,d) single-step, b,e) two-step, and c,f) three-step process.

The formation of a TiO_2 rutile oxide layer with an $\alpha\text{-Al}_2\text{O}_3$ top layer during air oxidation has been explained previously.^[15] After the two-step process, Ti_3Al grains are identified directly at the surface. As Al_2O_3 forms at the oxide–gas interface during the single-step process,^[15,31] a local Al enrichment occurs at the surface after the oxide layer reduction step. The formation of Ti_3Al is therefore plausible according to the Ti–Al–O phase diagram.^[44]

4.2. Surface Morphology and Roughness

The formation of elevated oxide grain clusters, which contribute to a roughness increase during oxidation in air, is observed elsewhere.^[10,13,15,31,45] Such oxide grain clusters (Figure 4d) are the reason for the large interquartile range observed during the oxide layer thickness evaluation (Figure 11) since they protrude up to about 2 μm from the rest of the surface. A mechanism of oxide

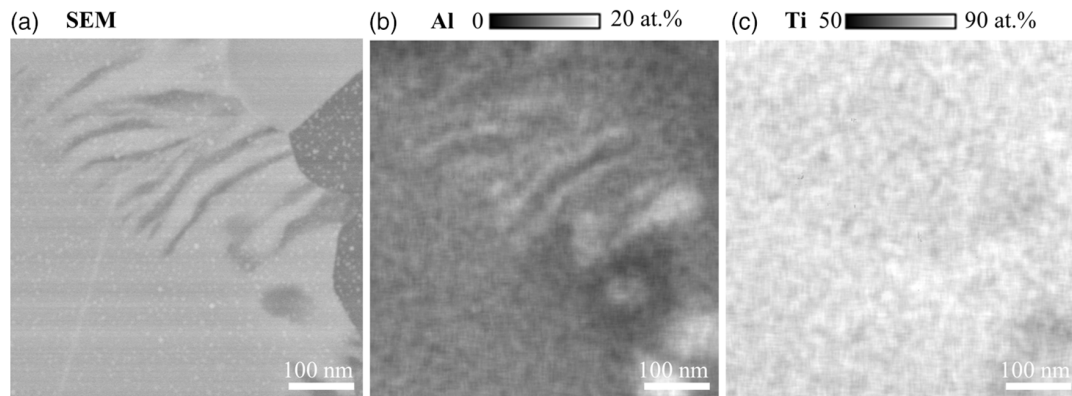


Figure 10. a) BSE SEM cross-sectional image of a region with lamellar structure (arrow 4, Figure 9 b)) occurring after the two-step process, with quantitative EDS mappings of b) aluminum and c) titanium.

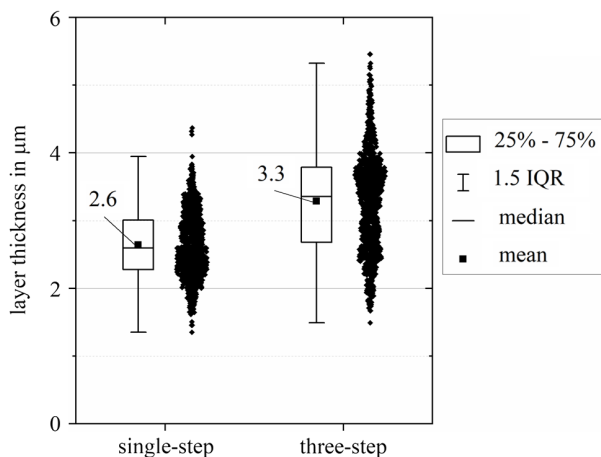


Figure 11. Oxide layer thickness after the single-step and three-step process, showing the mean, median, and interquartile range (IQR).

layer formation, proposed by Du et al.^[15] and discussed by Zhang et al.,^[31] cannot explain the formation of the observed clusters. This mechanism consists of the following steps: TiO₂ nuclei formation and subsequent surface coverage, TiO₂ rutile formation at the gas–oxide and oxide–substrate interface, and formation of nodular Al₂O₃ at the gas–oxide interface with a subsequent coverage. Based on the SEM-EDS cross-sectional analysis, the observed oxide grain clusters are not such Al₂O₃ nodes. Casadebaigt et al.^[46] reported that a Ti6Al4V specimen showed preferential oxide growth on β-laths, leading to oxide grain clusters similar to the ones observed, which provides a different explanation. After the two-step process, a terraced surface morphology is observed as Hertel et al.^[47] did in the case of commercially pure titanium. The observed morphology is therefore not related to the formation of Ti₃Al but influenced by the process parameters during the oxide layer reduction step.

4.3. Oxide Layer Growth Velocity

Despite similar process parameters during the oxide growing step, the three-step process leads to a thicker oxide layer. This

is because the roughness and the oxygen concentration at the surface are increased before the final oxidation step, which causes a faster oxide layer growth.

4.4. Subsurface Microstructure

In the case of the single-step process, a change in microstructure, such as a decrease of β-phase near the oxide–substrate interface,^[35] is barely visible. During the two-step process, a β-phase depleted zone of approximately 5 μm is visible. In this zone, also referred to as α-case, lamella consisting of Ti α-phase and Ti₃Al α₂-phase occur, as well as regions with Ti α-phase only. This is in agreement with Bagot et al.^[48] The β-phase depleted zone is followed by an α- and β-phase transition area, as described by Zhang et al.,^[35] until a region with stable α- and β-phase content is reached. Pores present in some specimens after the two-step process can be related to the Kirkendall effect.^[49] The microstructures in the subsurface regions after the two-step and three-step process are similar.

4.5. Oxygen Diffusion Zone

The oxygen diffusion zone after the single-step process is 20 μm deep. The oxygen concentration-depth profile shows a gradual decrease because it results from a process controlled by oxygen diffusion^[50] and therefore is a solution of the Fick's law.^[51] Thus, the diffusion coefficient of oxygen in Ti6Al4V D_C can be calculated from the oxygen concentration-depth profile $C(x)$ by solving

$$\frac{C(x) - C_S}{C_1 - C_S} = 1 - \operatorname{erf} \left[\frac{x}{2\sqrt{D_C t}} \right] \quad (4)$$

where C_1 is the oxygen concentration at the interface between oxide layer and diffusion zone, C_S is the initial oxygen concentration in the substrate, and t is the time of thermal oxidation, i.e., 16 h for the single-step process at 680 °C, yielding $D_C = 1.15 \pm 0.01 \times 10^{-16} \text{ m}^2 \text{ s}^{-1}$. The diffusion coefficient D_H derived from the corresponding microhardness-depth profile $H(x)$ can be calculated with the modified error function model as proposed by Vaché and Monceau^[43]

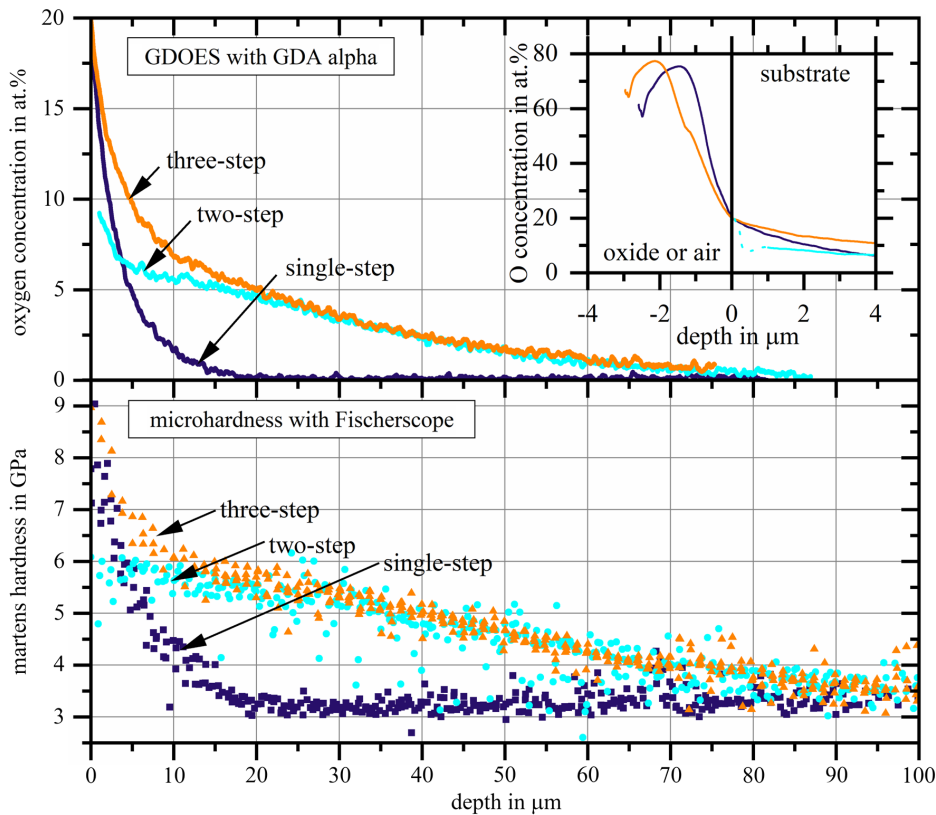


Figure 12. Oxygen concentration-depth and microhardness-depth profiles after the single-step, two-step, and three-step process starting from either the oxide-substrate (single- and three-step) or the substrate-air interface (two-step) as indicated in the excerpt.

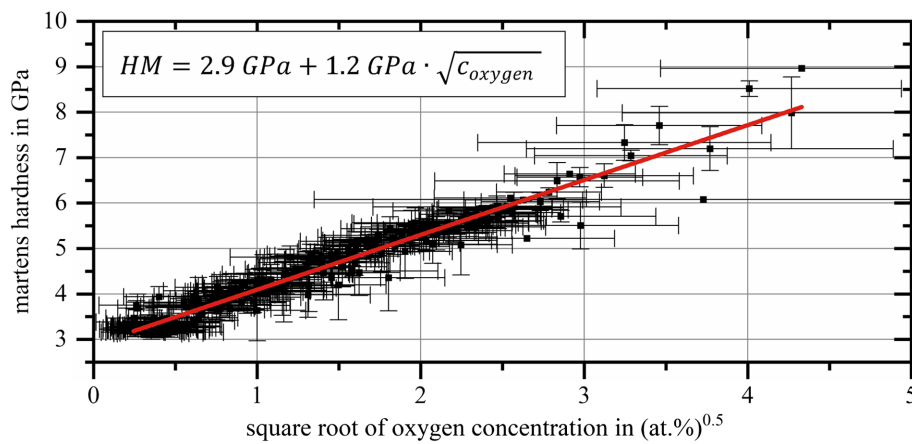


Figure 13. Correlation of Martens hardness and oxygen concentration in Ti6Al4V.

$$\frac{H(x) - H_S}{H_1 - H_S} = \sqrt{1 - \operatorname{erf}\left[\frac{x}{2\sqrt{D_H t}}\right]} \quad (5)$$

where H_1 is the hardness at the interface between oxide layer and diffusion zone and H_S is the initial hardness substrate, yielding $D_H = 2.0 \pm 0.1 \times 10^{-16} \text{ m}^2 \text{ s}^{-1}$. This is in good agreement

with the literature values determined for Ti6Al4V in a similar temperature range.^[52,53]

After the two-step process, the diffusion depth is enhanced to 85 μm . The reduced oxygen concentration at the gas-substrate interface compared with the single-step process indicates that the oxide layer completely dissolved before the end of the second process step and thus could no longer serve as oxygen reservoir.^[35] During the three-step process, the oxygen

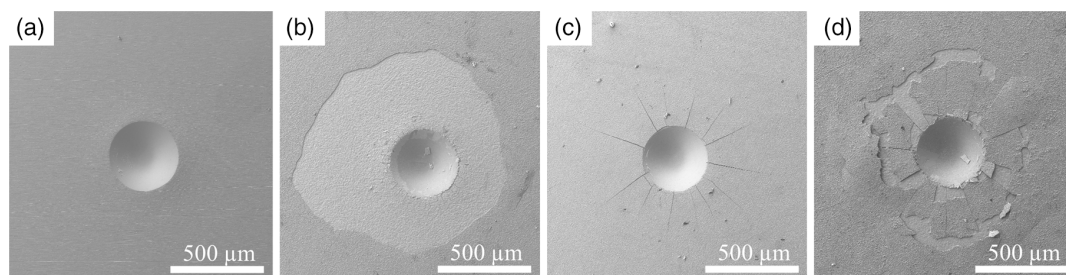
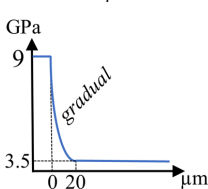
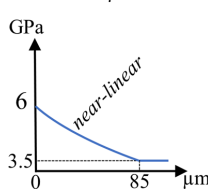
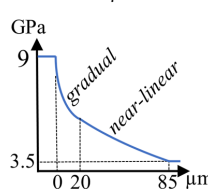


Figure 14. a) SE SEM images after Rockwell indentation testing of specimen surfaces in the initial state without an oxide layer, b) after the single-step process, c) the two-step process with no oxide layer present, and d) the three-step process.

Table 3. Impact of thermal oxidation process design on characteristic surface properties.

	Single-step	Two-step	Three-step
Presence of an oxide layer	Yes	No	Yes
Surface appearance	Brown	Mat metallic	Brown
Constitution of surface grains	TiO ₂ (rods or polyhedrons), α-Al ₂ O ₃	α ₂ -Ti ₃ Al	TiO ₂ (rods or polyhedrons), α-Al ₂ O ₃
Surface morphology	Nodular oxide grain clusters	Terrace structure	Nodular oxide grain clusters
Roughness	High	Medium	Highest
Layer growth velocity	Slower	Not applicable	Faster
Subsurface microstructure	α + β phase	→β depleted zone (α-Ti and α-Ti/α ₂ -Ti ₃ Al lamella) → transition area → α + β phase	→β depleted zone (α-Ti and α-Ti/α ₂ -Ti ₃ Al lamella) → transition area → α + β phase
Oxygen diffusion zone	20 μm	85 μm	85 μm
Hardness profiles (schematic) correlating to the oxygen concentration profiles according to Equation (3)			
Oxide layer adhesion	Class 3 (complete delamination)	Not applicable	Class 2 (partial delamination with layer segmentation)
Expected tribological behavior	Fair (hard oxide layer but danger of spallation)	Poor (no protecting oxide layer)	Best (hard oxide layer with better adhesion)

concentration at the oxide–substrate interface is enhanced, while the overall diffusion depth of the two-step process is maintained. In approximation, the oxygen concentration–depth profile achieved with the three-step process is a superposition of the profiles obtained with the single-step and two-step process and consists of a region with a pronounced gradual decrease near the oxide–substrate interface followed by a near-linear decrease.

4.6. Hardness Profiles

Because the hardness profiles correlate with the oxygen concentration–depth profiles, the three-step process not only allows to optimize the oxide layer thickness, the oxygen diffusion depth, and the oxygen concentration–depth profile, but also the

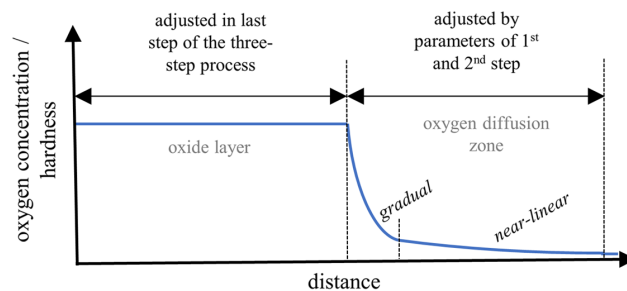


Figure 15. Schematic influence of the first, second, and third step of the three-step process on the obtained oxide layer thickness and oxygen diffusion zone depth.

microhardness–depth profile with regard to tribological applications (Figure 15).

4.7. Oxide Layer Adhesion

The oxide layer adhesion after the three-step process is improved compared with the single-step process, and the mechanism of delamination is different. While the oxide layer obtained during the single-step process spalls of instantaneously upon indentation, this is not the case for the three-step process. As the observed segmentation of the oxide layer is related to cracks present in the subsurface region, a bonding between the oxide layer and the substrate during the indentation process is present. The formation of cracks in the subsurface region of specimens after thermal oxidation is attributed to an increased hardness due to oxygen diffusion, accompanied by embrittlement.

5. Conclusion

Ti6Al4V was treated with three different thermal oxidation processes. An oxide layer grows on the substrate during a single-step process through oxidation in air (680 °C, 6 h). In a two-step process, this oxide layer vanishes during an appended solid-state reduction step under vacuum (850 °C, 16 h, sealed glass tube). In a three-step process, an additional oxide layer growing step in air is added (680 °C, 6 h).

1) The oxygen concentration- and the correlated hardness-depth profiles after the three-step process are a superposition of the profiles obtained after the first and second process step. The maximum possible oxygen concentration is reached at the oxide–substrate interface followed by a gradual decrease until a depth of 20 µm and a near-linear decrease until 85 µm.

2) The oxide layer adhesion after the three-step process is improved compared with simple oxidation in air.

3) Despite minor differences in oxide layer thickness and roughness, the outer most oxide layers obtained during the single-step and three-step process are similar. Therefore, the improved adhesion after the three-step process can be related to the optimized oxygen concentration-depth profile underneath the oxide layer.

Acknowledgement

The authors are grateful for the financial support of the German Research Foundation DFG (project number 270293189; GL181/41–2 and GA1704/12–2).

Open access funding enabled and organized by Projekt DEAL.

Conflict of Interest

The authors declare no conflict of interest.

Data Availability Statement

Research data are not shared.

Keywords

boost diffusion hardening, oxygen diffusion hardening, thermal oxidation, Ti–6Al–4V, titanium alloys

Received: July 8, 2021
Revised: August 23, 2021
Published online: September 15, 2021

- [1] G. Lütjering, J. C. Williams, *Titanium*, Springer-Verlag, Berlin Heidelberg **2007**.
- [2] H. Gülerüz, E. Atar, F. Seahjani, H. Çimenoglu, *Diffusion Foundations* **2015**, 4, 103.
- [3] K. G. Budinski, *Wear* **1991**, 151, 203.
- [4] M. C. Galetz, E. W. Fleischmann, C. H. Konrad, A. Schuetz, U. Glatzel, *J. Biomed. Mater. Res., Part B: App. Biomat.* **2010**, 93B, 244.
- [5] X. Liu, P. K. Chu, C. Ding, *Mater. Sci. Eng. R: Reports* **2004**, 47, 49.
- [6] D. G. Bansal, M. Kirkham, P. J. Blau, *Wear* **2013**, 302, 837.
- [7] M. C. Galetz, S. H. Seiferth, B. Theile, U. Glatzel, *J. Biomed. Mater. Res., Part B: App. Biomat.* **2010**, 93B, 468.
- [8] L. Mengis, C. Grimme, M. C. Galetz, *Wear* **2021**, 426, 341.
- [9] J. Ruzyllo, *Semiconductor Glossary: A Resource For Semiconductor Community*, WORLD SCIENTIFIC, New Jersey, London, Singapore, Beijing, ShanghaiHong Kong, Taipei, Chennai, Tokyo **2017**.
- [10] A. Biswas, J. Dutta Majumdar, *Mater. Characterization* **2009**, 60, 513.
- [11] A. Ashrafzadeh, F. Ashrafzadeh, *J. Alloys Compd.* **2009**, 480, 849.
- [12] H. Gülerüz, H. Cimenoglu, *Biomaterials* **2004**, 25, 3325.
- [13] S. Kumar, T. S. N. Sankara Narayanan, S. Ganesh Sundara Raman, S. K. Seshadri, *Mater. Chem. Phys.* **2010**, 119, 337.
- [14] S. Frangini, A. Mignone, F. de Riccardis, *J. Mater. Sci.* **1994**, 29, 714.
- [15] H. L. Du, P. K. Datta, D. B. Lewis, J. S. Burnell-Gray, *Corros. Sci.* **1994**, 36, 631.
- [16] H. Guleryuz, H. Cimenoglu, *J. Alloys Compd.* **2009**, 472, 241.
- [17] H. Dong, T. Bell, *Wear* **2000**, 238, 131.
- [18] S. Wang, Z. Liao, Y. Liu, W. Liu, *Mater. Chem. Phys.* **2015**, 159, 139.
- [19] M. Szota, A. Lukaszewicz, K. Kosinski, *Revista de Chemie* **2018**, 69, 2850.
- [20] C. Coddet, A. M. Craze, G. Beranger, *J. Mater. Sci.* **1987**, 22, 2969.
- [21] A. M. Chaze, C. Coddet, *J. Less Common Met.* **1990**, 157, 55.
- [22] J. T. Philip, J. Mathew, B. Kuriachen, *Friction* **2019**, 7, 497.
- [23] H. Okamoto, *J. Phase Equilib. Diffus.* **2011**, 32, 473.
- [24] J. Unnam, R. N. Shenoy, R. K. Clark, *Oxid. Met.* **1986**, 26, 231.
- [25] S. Zabler, *Mater. Charact.* **2011**, 62, 1205.
- [26] H. Dong, A. Bloyce, P. H. Morton, T. Bell, *Surf. Eng.* **1997**, 13, 402.
- [27] P. A. Dearnley, K. L. Dahm, H. Çimenoglu, *Wear* **2004**, 256, 469.
- [28] H. Guleryuz, H. Cimenoglu, *Surf Coat. Technol.* **2005**, 192, 164.
- [29] D. Xiong, Y. Yang, Y. Deng, *Surf Coat. Technol.* **2013**, 228, S442.
- [30] N. Lin, P. Zhou, Y. Wang, J. Zou, Y. Ma, Z. Wang, W. Tian, X. Yau, B. Tang, *Surf. Rev. Lett.* **2015**, 22, 1550033.
- [31] Y. Zhang, G.-R. Ma, X.-C. Zhang, S. Li, S.-T. Tu, *Corro. Sci.* **2017**, 122, 61.
- [32] L. Cao, J. Liu, Y. Wan, S. Yang, J. Gao, J. Pu, *Surf Coat. Technol.* **2018**, 337, 471.
- [33] R. Yazdi, H. M. Ghasemi, M. Abedini, C. Wang, A. Neville, *Tribol Lett* **2019**, 67, 445.
- [34] H. Dong, X. Y. Li, *Mater. Sci. Eng.: A* **2000**, 280, 303.
- [35] Z. X. Zhang, H. Dong, T. Bell, B. Xu, *J. Alloys Compd* **2007**, 431, 93.
- [36] Y. Zhou, Q. Y. Zhang, J. Q. Liu, X. H. Cui, J. G. Mo, S. Q. Wang, *Wear* **2015**, 344–345, 9.
- [37] H. Hornberger, C. Randow, C. Fleck, *Mater. Sci. Eng.: A* **2015**, 630, 51.
- [38] F. Omidbakhsh, A. R. Ebrahimi, S. H. Mousavi, R. A. Khosroshahi, S. Nazarpour, *Surf Coat. Technol.* **2011**, 205, 2954.
- [39] B. Bacroix, M. Lahmari, G. Inglebert, I. L. Caron, *Wear* **2011**, 271, 2720.
- [40] A. R. Rastkar, B. Shokri, T. Bell, *Surf Coat. Technol.* **2008**, 202, 6038.
- [41] M. Reif, F. Scherm, M. C. Galetz, U. Glatzel, *Oxid. Met.* **2014**, 82, 99.
- [42] M. Mosbacher, F. Scherm, U. Glatzel, *Surf Coat. Technol.* **2018**, 339, 139.

- [43] N. Vaché, D. Monceau, *Oxid. Met.* **2020**, *93*, 215.
- [44] A. Rahmel, M. Schütze, W. J. Quadackers, *Mater. Corros.* **1995**, *46*, 271.
- [45] E. Dong, W. Yu, Q. Cai, L. Cheng, J. Shi, *Oxid. Met.* **2017**, *88*, 719.
- [46] A. Casadebaigt, J. Hugues, D. Monceau, *Oxid. Met.* **2018**, *90*, 633.
- [47] C. Hertl, E. Werner, R. Thull, U. Gbureck, *Biomed. Mater.* **2010**, *5*, 54104.
- [48] P. A. J. Bagot, A. Radecka, A. P. Magyar, Y. Gong, D. C. Bell, G. D. W. Smith, M. P. Moody, D. Dye, D. Rugg, *Scripta Materialia* **2018**, *148*, 24.
- [49] F. Seitz, *Acta Metallurgica* **1953**, *1*, 355.
- [50] P. Kofstad, *High Temperature Corrosion*, Elsevier, London **1988**.
- [51] J. Crank, *The Mathematics Of Diffusion*, Clarendon Press, Oxford **1976**.
- [52] A. Casadebaigt, J. Hugues, D. Monceau, *Corrosion Sci.* **2020**, *175*, 108875.
- [53] N. Vaché, Y. Cadoret, B. Dod, D. Monceau, *Corrosion Sci.* **2021**, *178*, 109041.